Numerical Investigation of the Flow Around a Golf Ball at Around the Critical Reynolds Number and its Comparison with a Smooth Sphere

Li, Jing
Tsubokura, Makoto
Tsunoda, Masaya

(Citation)
Flow Turbulence and Combustion,95(2-3):415-436

(Issue Date)
2015-10

(Resource Type)
journal article

(Version)
Accepted Manuscript

Numerical Investigation of the Flow around a Golf Ball at around the Critical Reynolds Number and its Comparison with a Smooth Sphere

Jing Li · Makoto Tsubokura · Masaya Tsunoda

Abstract The flow over a stationary golf ball has been numerically investigated by conducting large-eddy simulations in the subcritical, critical and supercritical regimes. A direct comparison of features of flow fields was made to a smooth sphere model. Particular attention was paid to the effect that the golf ball dimples have on the development of lateral force and wake structures. In the subcritical regime, the lateral force varies irregularly in time for both the golf ball and the smooth sphere, and the wake structures of these two models appear to be similar, indicating the limited effect of the surface roughness on the flow behaviors in this regime. In the critical regime, both the golf ball and the smooth sphere exhibit a larger magnitude lateral force oscillation compared to the subcritical cases, while the wavelengths of the flow structures show differences between the golf ball and the smooth sphere. In the supercritical regime, both the golf ball and the smooth sphere are subjected to a nonzero lateral force during a long time interval. However, the magnitude of the lateral force acting on the golf ball is much smaller due to the relatively more concentrated and less asymmetric wake structures compared to the smooth sphere.

Keywords Golf ball · Sphere · Wake turbulence · Aerodynamics

Jing Li
Laboratory of Computational Fluid Mechanics, Faculty of Engineering, Hokkaido University, Sapporo, Hokkaido, 060-0808, Japan
e-mail: jingli@eis.hokudai.ac.jp

Makoto Tsubokura (✉)
Computational Fluid Dynamics Laboratory, Department of Computational Science, Graduate School of System Informatics, Kobe University, 1-1 Rokkodai, Nada-ku, Kobe, 657-8501, Japan
Complex Phenomena Unified Simulation Research Team, RIKEN Advanced Institute for Computational Science, 7-1-26 Minatojima-Minami-machi, Chuo-ku, Kobe, Hyogo 650-0047, Japan
e-mail: tsubo@tiger.kobe-u.ac.jp

Masaya Tsunoda
Research & Development HQ, Research Dept. 1, Sumitomo Rubber Industries, Ltd. 1-1, 2-chome, Tsutsui-cho, Chuo-ku, Kobe, 651-0071, Japan
e-mail: m-tsunoda.az@srigroup.co.jp

1 Introduction

Previous studies [1-3] have revealed that the dimples on a golf ball could lead to the drag crisis at Reynolds numbers remarkably lower than the typical critical Reynolds number of smooth sphere cases [4]. Interestingly, such lower Reynolds numbers are in the range where most golf tournaments are played [5]. Hence, to understand the aerodynamics of a golf ball might shed light on the science behind many other ball sports.

As one of the most basic and relevant topics to the research of golf balls, the investigation of the flow over a smooth sphere is often studied for a variety of different aspects. In the early stage, most of the works were completed using experimental methods. Achenbach [4, 6] directly investigated the drag crisis of a smooth sphere as well as the vortex shedding features by means of wind tunnel measurement. Taneda [7], Sakamoto and Haniu [8] subsequently observed the details of the wake structures and the vortex shedding patterns behind a sphere at various Reynolds numbers by the visualization of smoke and dyed water. More recently, owing to the improvement of computing technology, numerical methods have been increasingly applied to corresponding studies. Constantinescu and Squires [9] analyzed the flow field around a smooth sphere in both the subcritical and supercritical regimes by detached eddy simulation. They provided insight into both the statistical features, such as the prediction of the mean drag force, and the instantaneous features including how the aerodynamic forces developed over time. Muto et al. [10] extended the numerical work to the research on a rotating sphere. In this study, Large-eddy simulations (LES) were conducted for a sphere in both stationary and rotating conditions, and the phenomenon that a lift force pointing to the direction opposite to the one suggested based on the potential theory, which is namely the negative or inverse Magnus effect, was successfully reproduced and its physical mechanism was discussed.

Likewise, studies of the flow over a dimpled sphere were conducted mainly relying on experiments at the beginning. Davies [11] measured the aerodynamic forces on spinning golf balls by dropping them in a wind tunnel. Bearman and Harvey [1] measured the aerodynamic forces acting on golf balls with and without rotating motion in a wide Reynolds number range. Additionally, they estimated the aerodynamic performance of golf balls with different dimple patterns. Bearman and Harvey revealed two interesting phenomena. One is that the dimples reduce the drag at lower Reynolds numbers when compared to smooth sphere cases. The other is that drag force in the supercritical regime barely increases as the Reynolds number increases. Choi et al. [2] further investigated the mechanism of the drag reduction caused by the dimples on a sphere. They directly measured the streamwise velocity and its fluctuation above dimples in different positions using a hot-wire anemometer. Based on the results, Choi et al. proposed that the unstable shear layer developed after a local flow separation above the dimples increases the momentum of the flow in the near wall region; the high energy flow then experiences a local reattachment and consequently delays the complete flow separation. Due to the challenges of computing the flow past golf balls [12], the mechanism proposed by Choi et al. has not been numerically demonstrated until very recently. Smith et al. [3] conducted direct numerical simulations (DNS) for the flow over a stationary golf ball at the subcritical and supercritical Reynolds numbers. Their calculation results further solidified the process of the local separation and local reattachment.

In addition to the streamwise drag force, attention has been increasingly focused towards the lateral force components exerted on the spheres. Yun et al. [13] provided some insights into the time-dependent variation of the lateral forces acting on a smooth sphere in the subcritical regime using large eddy simulation. Constantinescu and Squires [9] further investigated the development of the lateral forces for both the subcritical and supercritical smooth sphere cases in their numerical works. Norman and McKeon [14] experimentally measured the fluctuating drag and lateral forces on a smooth sphere in various Reynolds number regimes. Moreover, Norman et al. [15-16] extended their research to rough spheres. They measured the aerodynamic forces respectively with a stationary and an azimuthally rotating stud being placed on the sphere surface.

For a golf ball, however, previous studies primarily focused on how the dimples help to reduce the drag force and consequently increase the flying distance. The effect of the dimples on the lateral force components was rarely discussed in previous literatures. Actually, a golfer expects not only the long flying distance but also the precise flying trajectory in the games, and the lateral forces exerted on the golf ball could strongly affect its flying path. Therefore to gain insights into how the dimples affect the lateral forces would be beneficial to further understanding a golf ball’s performance.

Another interesting issue of concern is the influence of the surface roughness introduced by the dimples on the wake flow field. Perry et al. [17-19] conducted several experiments concerning the flow issued from an oscillating glass tube, and they indicated the response of the coherent wake structures to small perturbations at low Reynolds numbers. However, the wake flow structure behind the golf ball and its comparison with the smooth sphere has not been investigated in detail.

Therefore, the main objective of the present study is to gain insights into how the surface roughness introduced by the dimples on a golf ball affects the lateral force components and the wake structures at around the critical Reynolds number. Specifically, large-eddy simulations (LES) are performed on a stationary golf ball in the subcritical, critical and supercritical regimes, and the results are directly compared with the corresponding smooth sphere cases based on Muto's [10] model.

2 Simulation Overview

2.1 Numerical methods and conditions

In the present study, the spatially filtered continuity and Navier-Stokes equations for incompressible flow are solved as the governing equations in the LES:

$$\frac{\partial \overline{u}_i}{\partial x_i} = 0 \tag{1}$$

$$\frac{\partial \overline{u}_i}{\partial t} + \frac{\partial}{\partial x_j}\overline{u}_i\overline{u}_j = -\frac{\partial \overline{P}}{\partial x_i} + 2\frac{\partial}{\partial x_j}(\nu + \nu_{SGS})\overline{S}_{ij} \tag{2}$$

$$\overline{P} = \overline{p}/\rho + (\overline{u_i u_i} - \overline{u}_i\overline{u}_i)/3 \tag{3}$$

where u_i, p, ρ and ν are respectively the i-th velocity component, pressure, density and kinematic viscosity of the fluid. The strain rate tensor S_{ij} is defined as:

$$\overline{S}_{ij} = \frac{1}{2}\left(\frac{\partial \overline{u}_j}{\partial x_i} + \frac{\partial \overline{u}_i}{\partial x_j}\right) \tag{4}$$

The dynamic Smagorinsky model [20] is applied in this research. The governing equations are discretized based on the vertex-centered finite volume method. Meanwhile, the second-order central difference scheme is used for the spatial derivatives with 5% of the first-order upwind scheme being blended for the calculation of the convection term for the sake of numerical stability. For the time advancement, the first-order Euler implicit scheme is used, which coincides with the corresponding scheme in Muto's [10] work. According to the estimation provided by Muto et al [10], the simulation results showed very limited difference between the first-order Euler scheme and the third-order Adams-Moulton scheme when relatively fine meshes were allocated around the sphere and the Courant number was kept to be less than 1.8. In the present study, the Courant number is controlled to be less than 1.1. The Simplified Marker and Cell (SMAC) approach is used for the coupling of the pressure and velocity fields.

The target Reynolds numbers for the golf ball cases in the present research are respectively 4.3×10^4 for the subcritical regime, 7.5×10^4 for the critical regime, and 1.1×10^5, 1.7×10^5 for the supercritical regime. Here the Reynolds number is defined as Re=UD/ν, where U is the incoming flow velocity, D is the diameter of the golf ball, and ν is the kinematic viscosity. The numerical source code used in this study is the open source CFD code "FrontFlow/red" [21] which was originally developed in our research group.

2.2 Geometry and numerical grid

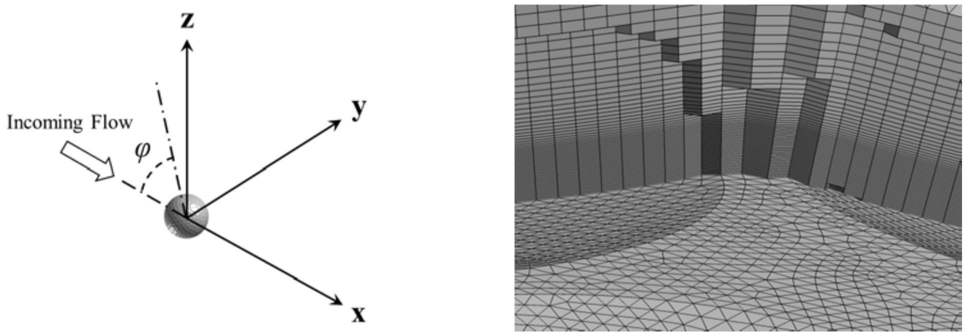

Fig.1 Coordinate system and the mesh details around the golf ball surface

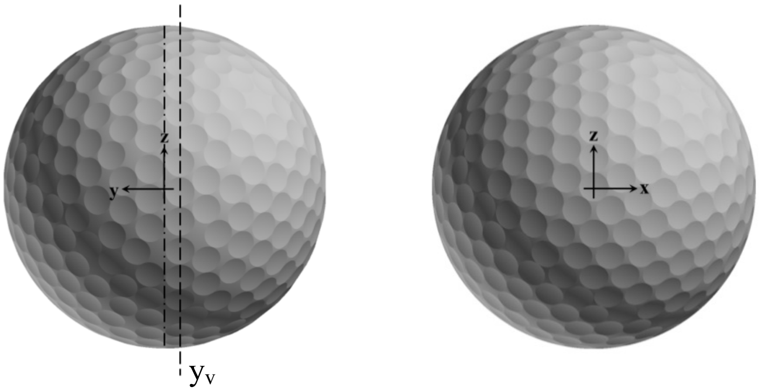

Fig.2 Geometry details of the golf ball

Shown in Fig.1 is the Cartesian coordinate system adopted in the present study with the center of the golf ball being placed at the position (x, y, z) = (0, 0, 0). Here, we define the x, y and z direction as the streamwise direction (from –x to +x), side force direction and lift force direction respectively. And we define the angle φ as the polar angle on the x-z plane measured from the front stagnation point of the golf ball. The azimuthal direction considered in this study is on the y-z plane.

Geometry details of the golf ball used in the current contribution is displayed in Fig.2 through the y-z view and x-z view of the golf ball model. 392 uniform-sized spherical dimples are distributed on the golf ball surface. The diameter of the dimples equals approximately 9.0×10^{-2} D, where D is the diameter of the golf ball. The dimensionless geometry parameter k/D, which quantitatively measures the surface roughness of the golf ball, is approximately 0.5×10^{-2}, where k represents the dimple depth. As also indicated in Fig.2, the path along the central joint line of the golf ball at y=0 does not go across any dimples on the golf ball surface. The plane y_v shown in Fig.2 is located at $y\approx-4.7\times10^{-5}$ D. This plane intersects the center of the row of dimples closest to the central joint line of the golf ball, and is used as the visualization plane for some of the interpretations discussed in following sections.

An unstructured finite volume grid is used for the present simulations. In particular, triangular elements are generated on the golf ball surface for properly reproducing the dimple details, and prism layers are allocated along the normal-wall direction starting from the surface mesh. To accurately capture the boundary layer separation and turbulence transition, the numerical grid around the golf ball must be of sufficient resolution [3, 10]. In the present study, the surface mesh size on the dimple edges is set to be approximately 2.34×10^{-3} D. There are about 40 triangular elements across the dimples and about 28 prism layers being generated within the distance of dimple depth k. The total cell number amounts to around 145 million. Some details about the numerical grid in the vicinity of the dimples are shown in Fig.1. Actually, the grid resolution applied here is much higher than that reported in Muto's [10] smooth sphere cases. In their study, the grid resolution was determined based on the laminar boundary-layer thickness δ_B measured at 90° from the front stagnation point of a sphere [10, 22]. For the calculations of their smooth sphere cases, the spatial resolution in the circumferential direction was set to be equal to δ_B, whereas the thickness of the first prism layer was about 1/20 δ_B.

However, even for the δ_B estimated with the highest Reynolds number considered in this work, the surface mesh resolution for the golf ball is smaller than 1/2 δ_B, and the thickness of the first prism layer is about 1/28 δ_B.

The computations are conducted in a rectangular duct with $-13 \leqslant x/D \leqslant 13$, $-5.6 \leqslant y/D \leqslant 5.6$ and $-5.6 \leqslant z/D \leqslant 5.6$. The blockage ratio between the projection area of the golf ball and the cross-section of the domain is less than 0.63%. At the inlet boundary, a uniform velocity profile is imposed. At the outflow boundary, the gradient-free condition for the velocity and pressure is used. For the side-walls of the computation domain, a free-slip condition is applied. On the golf ball surface, since the required grid resolution in the vicinity of the surface is not clear, the velocity profiles which are initially assumed to follow the two-layer law (linear or log law depending on the normal-wall distance away from the boundary surface) are used to estimate the surface friction as a velocity boundary condition. After the simulation, the distance of the first nearest grid point from the boundary surface was checked a posteriori to validate the accuracy near the wall, and it was found that the y+ value in wall coordinate was less than 1.0 on almost the whole boundary surface (more than 99% areas) in the supercritical Reynolds number case. Thus it turns out that the boundary condition is actually equivalent to the no-slip condition. In fact, as shown in Fig.9, the velocity profile asymptotically becomes zero as the distance from the surface approaches zero.

3 Results

3.1 Statistical features

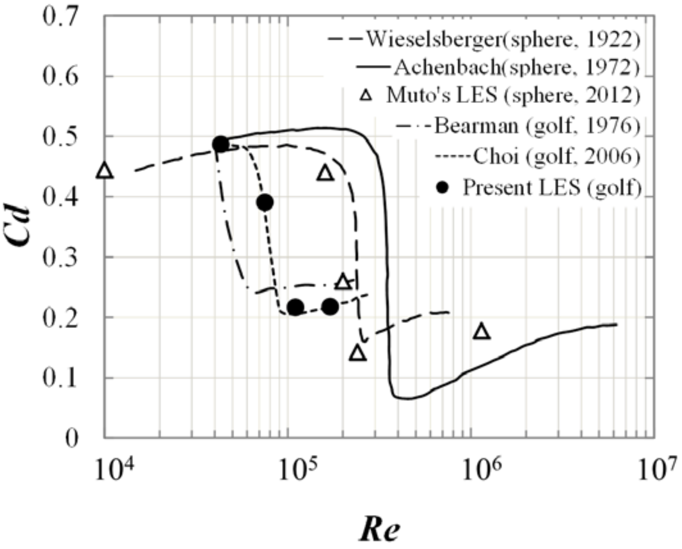

Fig.3 Comparison of the drag coefficients for golf balls and smooth spheres; Lines: experimental results; Symbols: numerical simulation results.

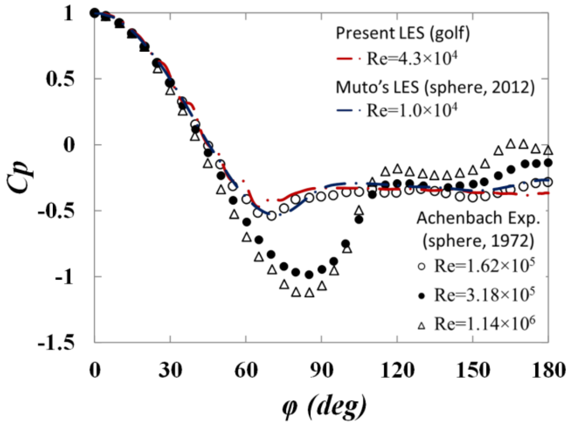

(a)

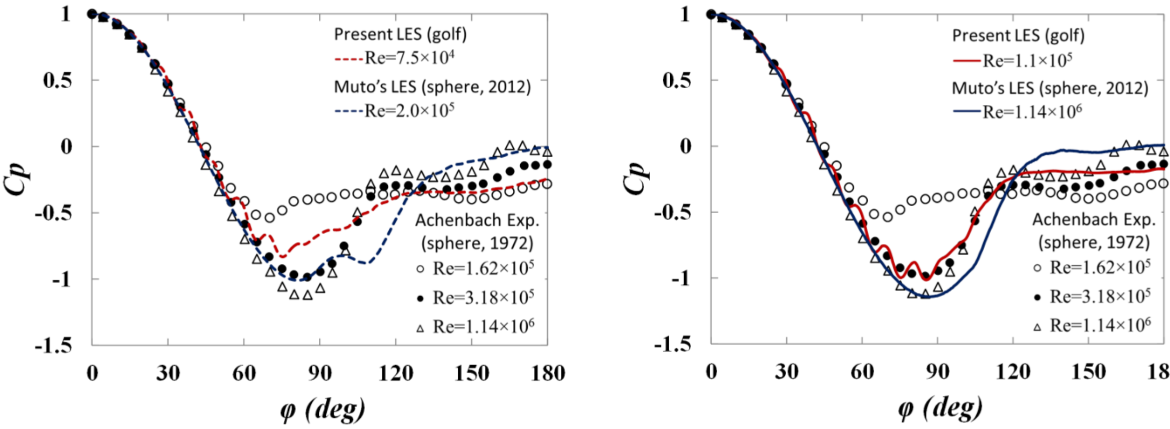

(b) (c)

Fig.4 Comparison of the time-averaged surface pressure distribution on the golf ball and the smooth spheres in the (a) subcritical regime; (b) critical regime; (c) supercritical regime. Lines: numerical simulation results; Symbols: experimental results.

Fig.3 shows the drag coefficient of the golf ball obtained by the present LES. The drag coefficient is defined as $Cd=2F_D/(\rho AU^2)$, where F_D, ρ, A, and U are respectively the drag force, density of the fluid, projected frontal area of the golf ball/smooth sphere, and the incoming flow velocity. Correspondingly, the side force and the lift force coefficients considered in the present study are respectively defined as $Cs=2F_S/(\rho AU^2)$ and $Cl=2F_L/(\rho AU^2)$, where F_S represents the side force along the y axis and F_L represents the lift force along the z axis. The results reported previously for both the golf ball cases [1-2] and the smooth sphere cases [4, 10, 23] are also included in Fig.3 as references. In order to examine the effect of the subgrid-scale model on the simulation results, a calculation without using any turbulence models was also conducted for the golf ball at $Re=1.1\times10^5$ (supercritical) based on the same numerical grid and the same settings of other numerical conditions. Comparing the results obtained without using any turbulence models to the corresponding results by LES at the same Reynolds number, an almost identical Cd value and flow field in the vicinity of the golf ball surface between the two cases is shown. Therefore, it can be concluded that, in the vicinity of the golf ball surface where the high resolution numerical grid is allocated, the effect on the corresponding areas imposed by the subgrid-scale model used in the present LES is insignificant. However, in the areas away from the golf ball where the grid resolution decreases, the utilization of the subgrid-scale model is very important for properly calculating the turbulence features of the flow.

As indicated in Fig.3, the considerable decrease of the drag force has been successfully captured for the golf ball in our simulations. The drag coefficient of the golf ball stays at around 0.49 at the subcritical Reynolds number ($Re=4.3\times10^4$), which is close to the value for the smooth sphere case in the same regime [4], and then decreases sharply by approximately 55% after the drag crisis, reaching to around 0.22 at the supercritical Reynolds number ($Re=1.1\times10^5$). However, as the Reynolds number further increases ($Re=1.7\times10^5$) in the supercritical regime, the drag coefficient stays at an almost constant value. This trend agrees very well with the experimental measurements by Bearman and Harvey [1] and Choi et al. [2]. It is also obviously shown in Fig.3 that the drag crisis of the present golf ball occurs at a considerably lower Reynolds number than with the smooth spheres. One can clearly observe that the drag coefficient of the golf ball at $Re=1.7\times10^5$ has already reduced by nearly 50% when compared to the smooth sphere case conducted by Muto et al. [10] at a similar Reynolds number ($Re=1.6\times10^5$).

In particular, the dimensionless parameter k/D of the golf ball is considered as one of the essential factors affecting the supercritical drag coefficient and the critical Reynolds number range in which the drag crisis occurs [1-3]. Actually, the golf ball used in the present study has the relative dimple depth ($k/D=0.5\times10^{-2}$) very close to that of Choi's [2] golf ball model ($k/D=0.4\times10^{-2}$), but much smaller than that of Bearman's [1] golf ball model ($k/D=0.9\times10^{-2}$). On the other hand, as clearly indicated in Fig.3, the simulation results obtained in the present study, as expected, show a good agreement with Choi's [2] experimental measurements concerning the critical Reynolds number range and the supercritical drag coefficients, which further demonstrate the high accuracy of the present numerical study.

The time-averaged surface pressure distributions of the golf ball are plotted in Fig.4, with the pressure distributions of the smooth spheres [4, 10] being included for comparison. The pressure coefficient is defined as $Cp=p/(0.5\rho U^2)$, where p is the pressure acting on the golf ball/smooth sphere. Particularly, the distribution for the golf ball cases are obtained in the section y=0 along the central joint line of the golf ball.

At the subcritical Reynolds number ($Re=4.3\times10^4$), the pressure distribution of the golf ball appears to be quite similar to the distributions of the smooth spheres in the same regime. As the Reynolds number goes into the critical range, the pressure profile drops quickly for both the golf ball and the smooth spheres due to the delay in flow separation. For the supercritical case ($Re=1.1\times10^5$), the pressure profile of the present golf ball compares well with the experimental data of the smooth sphere obtained by Achenbach at $Re=3.18\times10^5$ regarding the minimum value of Cp and its angular position. Such agreement also evidences the similarity of the drag coefficients between these two cases, as shown in Fig.3. Additionally, the Cp value of the golf ball shows some local fluctuation at several angular positions before it approaches the minimum value. Such variation is mainly affected by the dimples distributed in the vicinity of the central joint line.

3.2 Flow visualizations around the spheres

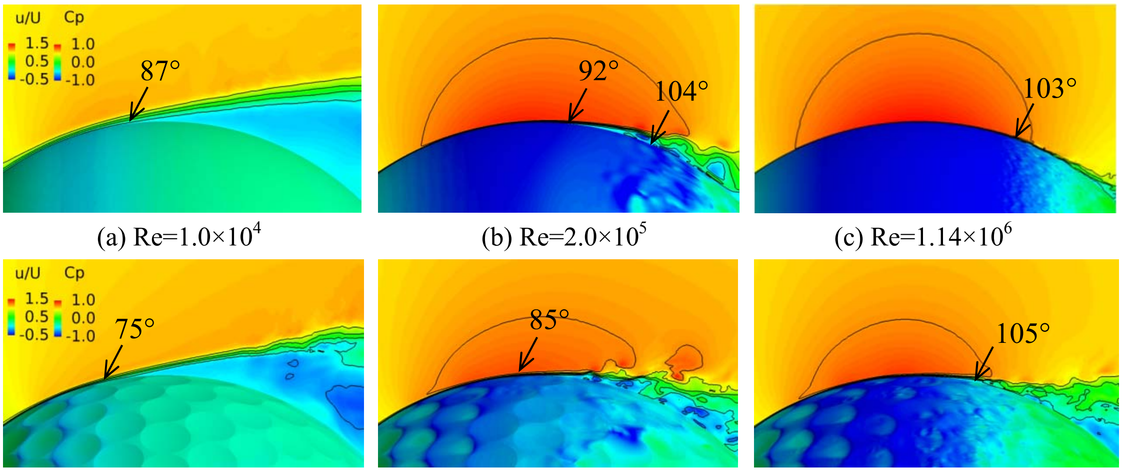

(a) $Re=1.0\times10^4$ (b) $Re=2.0\times10^5$ (c) $Re=1.14\times10^6$

(d) $Re=4.3\times10^4$ (e) $Re=7.5\times10^4$ (f) $Re=1.1\times10^5$

Fig.5 Instantaneous surface pressure distribution and contours of the instantaneous non-dimensional velocity distribution around the separation point at section y=0

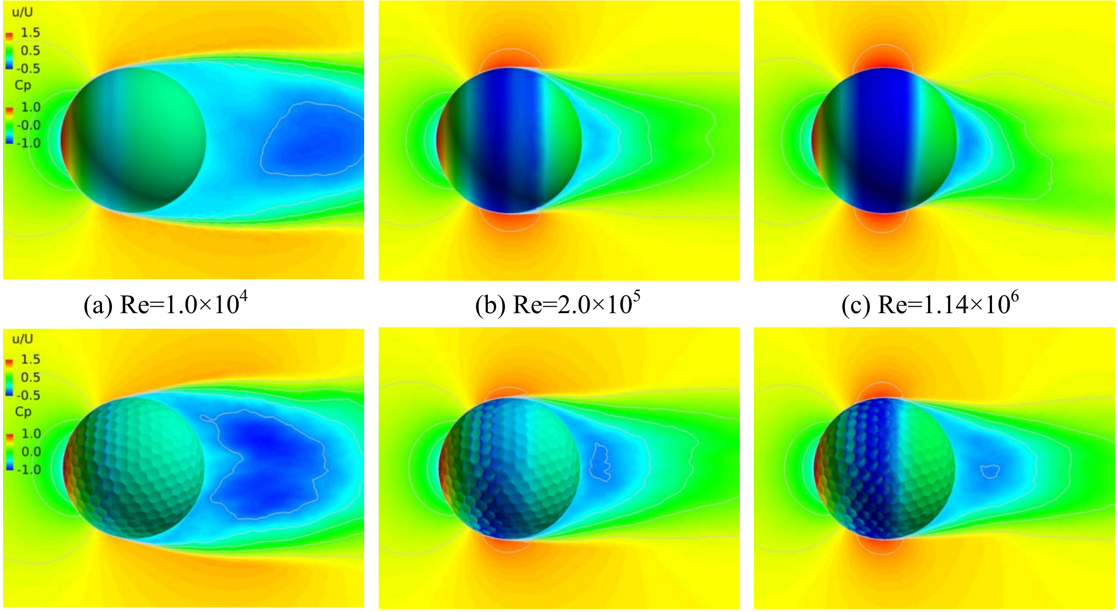

(a) $Re=1.0\times10^4$ (b) $Re=2.0\times10^5$ (c) $Re=1.14\times10^6$

(d) Re=4.3×10^4 (e) Re=7.5×10^4 (f) Re=1.1×10^5

Fig.6 Time-averaged surface pressure distribution and non-dimensional velocity distribution in the wake area at section y=0

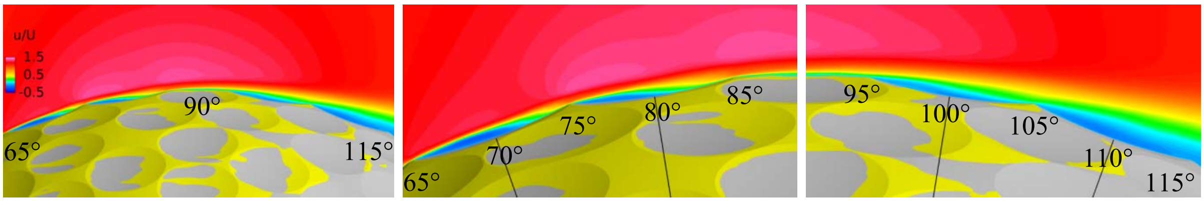

(a) (b) (c)

Fig.7 Time-averaged streamwise velocity around the dimples at Re=1.1×10^5 viewed on the y_v plane: (a) complete view from 65° to 115°; (b) detailed view from 65° to 90°; (c) detailed view from 90° to 115°; the parts of the golf ball surface colored by 'yellow' represent a positive streamwise velocity on the prism layer cell attached on the boundary surface, indicating a flow attachment at corresponding areas; the parts colored by 'gray' represent a negative streamwise velocity on the prism layer cell attached on the boundary surface, indicating a flow detachment at corresponding areas.

Fig.5 displays the instantaneous flow field (pressure coefficient Cp and non-dimensional velocity magnitude u/U, where u represents the streamwise velocity) around the separation point for the present golf ball and the smooth sphere model used by Muto et al. [10], with the arrows indicating the angular positions (value of φ) of the flow separations. The boundary layer separation is determined at the point where the streamwise velocity of the prism layer cell attached on the sphere surface becomes negative. For the smooth sphere, the separation point shifts downstream from around 87° at the subcritical Reynolds number to around 103° at the supercritical Reynolds number. Compared to the smooth sphere, however, the separation point of the golf ball varies more along the azimuthal direction due to the existence of surface roughness. In the subcritical regime, the separation point of the golf ball differs from 75° to 85° depending on the specific dimple distributions at different azimuthal positions. Correspondingly, the separation point varies azimuthally between 85° and 95° in the critical regime, and from 105° to 110° in the supercritical regime. A similarity between the flow field around the golf ball and the flow field around the smooth sphere can be observed for the subcritical cases, which suggests a limited effect of the dimples on the laminar boundary layer separation. However, the dimples do indeed lead to the turbulent boundary layer separation occurring at a lower Reynolds number for the golf ball comparing the results shown in Fig.5 (c) and (f). Particularly, two separation points at different angular positions were reported by Muto et al. [10] for the critical smooth sphere case (Re=2.0×10^5) due to the existence of the global separation bubble. For the golf ball, however, the separation bubble exists locally inside individual dimples, as displayed in Fig.7.

Shown in Fig.6 are the time-averaged pressure distribution on the sphere surfaces and velocity component in the streamwise direction in the flow fields. One can clearly observe that the width of the wake area for the golf ball stays comparable to that for the smooth sphere in the subcritical regime, again indicating the similar flow behavior between these two cases. As the Reynolds number increases, the wake region shrinks remarkably for both the golf ball and the smooth sphere as a result of the delay in the flow detachment, which consequently leads to the decrease of the drag coefficient.

Fig.7 depicts more details of the flow behavior as it traverses the dimples on the golf ball surface under the high Reynolds number condition. The time-averaged streamwise velocity obtained in a section across the center of the dimples is displayed in the figure with increasing φ values. As revealed by the visualization, the flow detaches locally at around 65° while passing the leading edge of the dimple, whereas it reattaches to the boundary again downstream before exiting the dimple at around 75°. These behaviors repeat again when the flow travels to the next dimple at around 80°. Due to the local reattachment occurring on the rear part of the previous dimple, the flow stays attached to the golf ball surface at around 90°, and it ultimately reaches full detachment at around 105°.

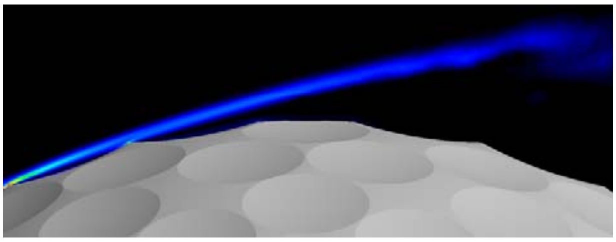

(a) Re=4.3×10^4

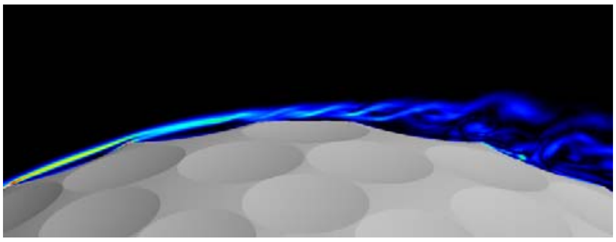

(b) Re=7.5×10^4

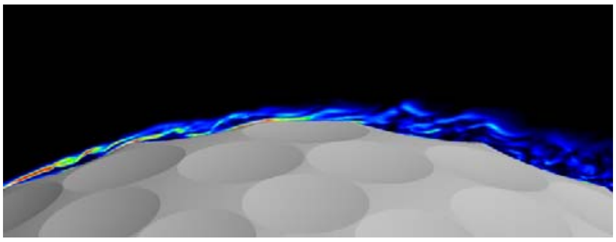

(c) Re=1.1×10^5

Fig.8 Contours of the instantaneous azimuthal vorticity viewed on the y_v plane at different Reynolds numbers; the vorticity direction is out-of-plane

Further insight into the flow near the dimples is provided in Fig.8 by visualizations of the instantaneous azimuthal vorticity perpendicular to the visualization plane y_v at different Reynolds numbers. For the subcritical case, the shear layer developed after the complete flow detachment shows relatively little instability until travelling some distance downstream from the separation point. For the critical case, the flow near the golf ball starts to become unstable as it exits the dimple close to the location of full separation. For the supercritical case, however, the flow appears to exhibit some variation as it traverses the dimples at more upstream positions. The shear layers developed following the local separation on the leading edge of the dimples quickly become unstable and small-scale vortices are generated within the dimples. Similar local separation characteristics were also reported by Choi et al. [2] and Smith et al. [3]. The unstable flow behavior results in a momentum increase of the near-wall flow and the consequent local reattachment inside the golf ball dimples. With the increased momentum, the flow could overcome the adverse pressure gradient and travel further downstream, which consequently delays the complete flow detachment. This mechanism is also considered as the key factor helping to lower the critical Reynolds number range for golf balls [2-3].

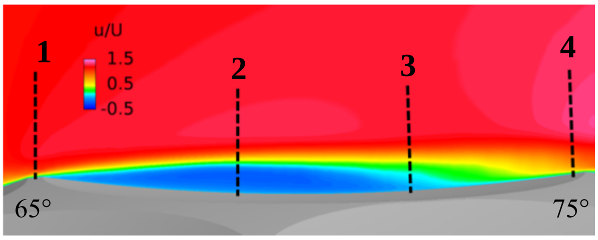

(a)

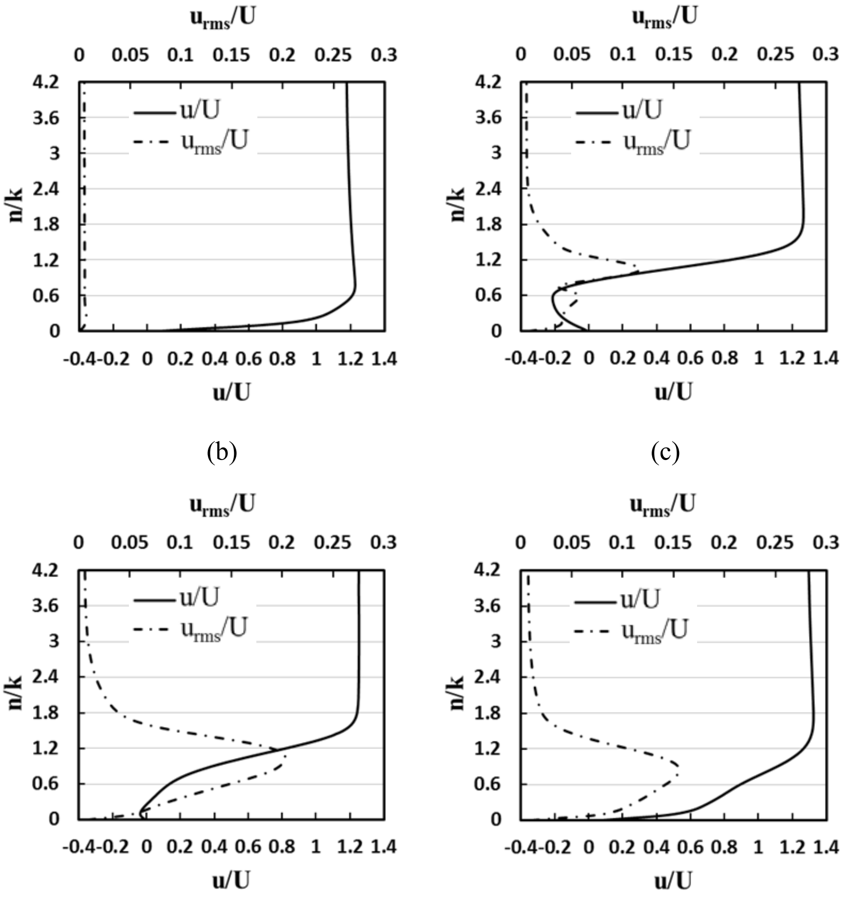

(b) (c)

(d) (e)

Fig.9 Profiles of the time-averaged streamwise velocity and the r.m.s fluctuation of streamwise velocity measured above a dimple: (a) positions 1-4 for profile plotting, shown in background is the mean streamwise velocity at Re=1.1×10^5; (b) profiles at position 1; (c) profiles at position 2; (d) profiles at position 3; (e) profiles at position 4

A quantitative clarification of the momentum transfer inside the dimples is plotted in Fig.9 for the supercritical case (Re=1.1×10^5). The time-averaged streamwise velocity and its root-mean-square fluctuation were measured at the four specific positions within the dimple at around 70° along the normal-wall direction, as shown in Fig.9 (a). A dimensionless normal-wall axis is used for displaying the profile, in which the variable n represents the normal-wall distance away from the boundary surface and k is the dimple depth. As illustrated in the figure, the flow stays attached while passing the leading edge of the dimple at position 1, and the flow velocity barely fluctuates. At position 2, the velocity profile is reversed in a small area near the boundary surface because of the local separation. At the same time, the velocity fluctuations significantly increase along the shear layer. Owing to the momentum transfer caused by the velocity fluctuations, the flow subsequently reattaches to the boundary surface and forms a separation bubble around position 3. The reattached flow with high momentum in the near-wall region further travels to position 4 and exits the dimple without any other local detachment. This process and the profiles shown in Fig.9 qualitatively agree well with the measurements by Choi et al. [2] and Smith et al. [3].

3.3 lateral force features and wake structures

Table 1 Summary of the time-averaged mean value and standard deviation (s.d.) of the side force coefficient Cs and lift force coefficient Cl for the golf ball and smooth sphere at the subcritical, critical and supercritical regime

		Golf Ball			Smooth Sphere		
		Re=4.3×10^4 (subcritical)	Re=7.5×10^4 (critical)	Re=1.1×10^5 (supercritical)	Re=1.0×10^4 (subcritical)	Re=2.0×10^5 (critical)	Re=1.14×10^6 (supercritical)
Cs	mean	-0.0392	0.0100	0.0460	-0.0222	0.0039	-0.0044
	s.d.	0.0461	0.0965	0.0399	0.0300	0.0601	0.0952
Cl	mean	0.0006	-0.0341	-0.0287	-0.0190	0.0137	-0.1425
	s.d.	0.0365	0.0643	0.0451	0.0292	0.0436	0.0549

3.3.1 Subcritical regime

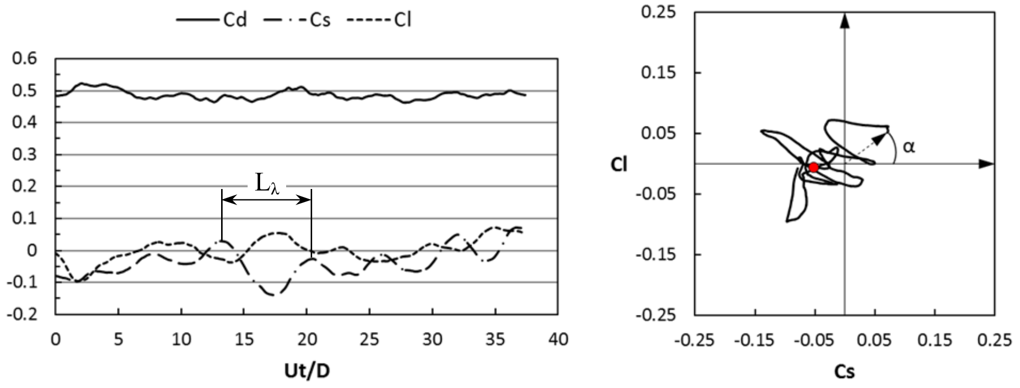

(a) (b)

Fig.10 Time series of the streamwise and lateral force coefficients for the golf ball at subcritical Re=4.3×10^4 after the flow reached statistically steady state: (a) temporal evolution of the drag coefficient Cd, side force coefficient Cs and lift coefficient Cl; L_λ represents the typical wavelength of the oscillating curves; (b) phase diagram of Cs and Cl, the red point represents the resultant lateral force at the non-dimensional moment indicated in Fig.12; the angle α indicates the instantaneous direction of the resultant lateral force looking from the downstream view of the spheres.

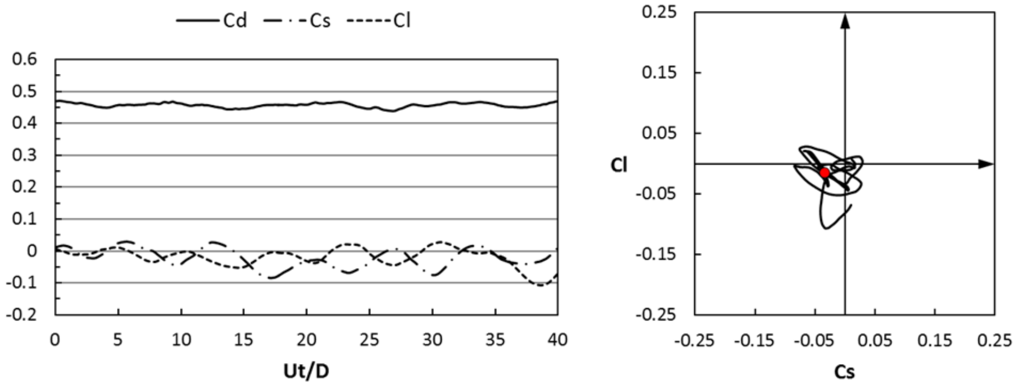

(a) (b)

Fig.11 Time series of the streamwise and lateral force coefficients for the smooth sphere at subcritical Re=1.0×10^4 after the flow reached statistically steady state: (a) temporal evolution of the drag coefficient Cd, side force coefficient Cs and lift coefficient Cl; (b) phase diagram of Cs and Cl, the red point represents the resultant lateral force at the non-dimensional moment indicated in Fig.13.

Time histories of the streamwise and lateral forces on the golf ball at Re=4.3×10^4 are provided in Fig.10, whereas the corresponding force evolution obtained using Muto's [10] smooth sphere model at

Re=1.0×10^4 is shown in Fig.11. For a better comparison, the dimensionless time scale Ut/D is used, where U is the incoming flow velocity, t is the real time and D is the diameter of the golf ball or smooth sphere. For all the time history data displayed in this paper, Ut/D=0 indicates a moment when the flow has reached a statistically steady state and a stable drag coefficient Cd. Such a process required calculations for at least tens of D/U time units [9] from the initial conditions depending on different Reynolds numbers. The phase diagram shown in Fig.10 (b)/Fig.11 (b) illustrates the evolution of the resultant lateral force within the same time interval shown in Fig.10 (a)/Fig.11 (a). As mentioned before, the side force (Cs) direction denotes the y-axis direction whereas the lift force (Cl) direction denotes the z-axis direction. The distance between the origin in the phase diagram (Cs=0, Cl=0) and a point on the curve (e.g. the length of the vector shown in Fig.10 (b)) represents the magnitude of the resultant lateral force coefficient (calculated by $\sqrt{Cs^2 + Cl^2}$) at a specific moment. The angle α shown in Fig.10 (b) indicates an instantaneous direction of the total lateral force looking from the downstream view of the spheres. The measurement L_λ shown in Fig.10 (a) indicates the typical wavelength of the oscillations of the lateral force components. Table 1 summarizes the time-averaged values and the standard deviations of the side and lift force coefficients for the golf ball and smooth sphere in various Reynolds number regimes.

As revealed in Fig.10, both the magnitude and the direction of the resultant lateral force vary irregularly in time for the golf ball at Re=4.3×10^4. Similar features are also evident in Fig.11 for the smooth sphere at Re=1.0×10^4, which agrees very well with the conclusions by Constantinescu et al. [9] and Yun et al. [13] regarding the flow over smooth spheres at the same Reynolds number. For both the golf ball and the smooth sphere, the mean values of the lateral force components are close to zero over an adequately long time interval. However, comparing Fig.10 (b) and Fig.11 (b), one can also observe that the curve in the phase diagram for the smooth sphere is relatively more concentrated around the origin, indicating that the magnitude and oscillation of the lateral force on the smooth sphere is slightly smaller than that of the golf ball, as also quantitatively evidenced in table 1.

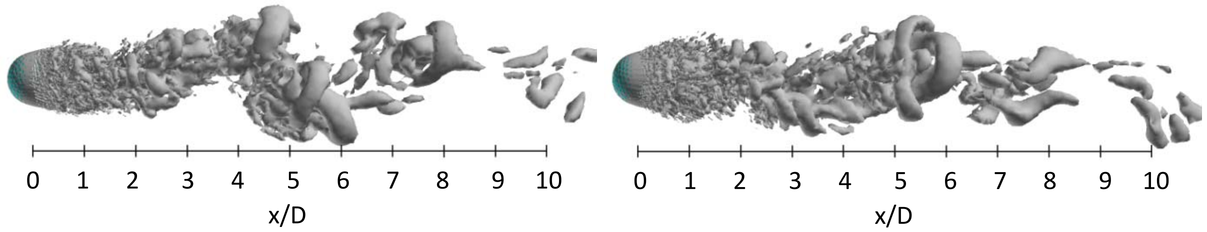

(a) x-y plane (b) x-z plane

Fig.12 Instantaneous vortical structures in the wake area of the golf ball at Re=4.3×10^4 (Ut/D=21.5, the resultant lateral force at this moment is indicated in Fig.10 (b) by the red point)

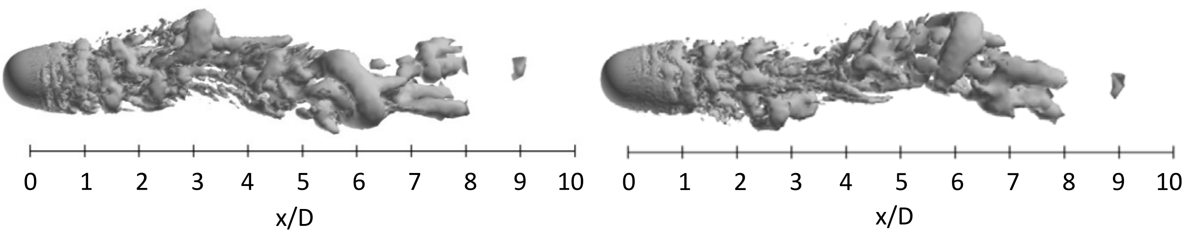

(a) x-y plane (b) x-z plane

Fig.13 Instantaneous vortical structures in the wake area of the smooth sphere at Re=1.0×10^4 (Ut/D=21.5, the resultant lateral force at this moment is indicated in Fig.11 (b) by the red point)

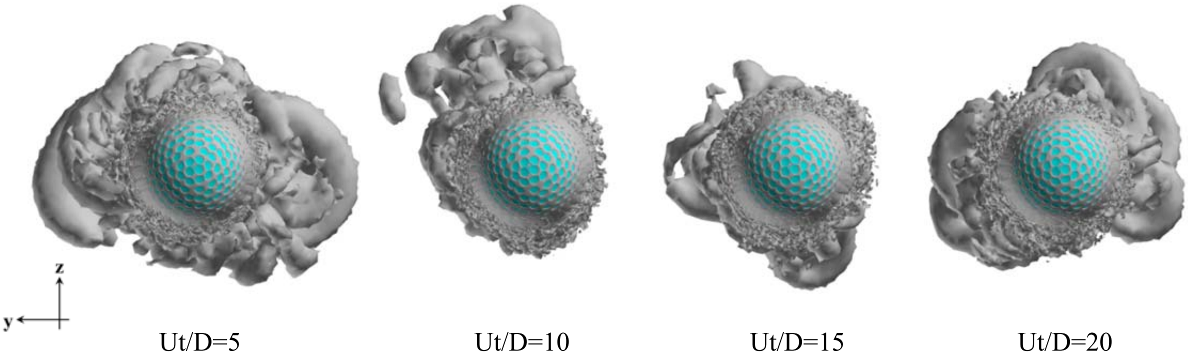

Ut/D=5 Ut/D=10 Ut/D=15 Ut/D=20

Fig.14 Instantaneous vortical structures of the golf ball at Re=4.3×10^4 visualized from the upstream view

Fig.12 and Fig.13 respectively show the instantaneous vortical structures in the wake area of the golf ball and the smooth sphere using the Q-criterion method [24]. Visualizations were obtained in two perpendicular planes. For the flow past a smooth sphere at subcritical Reynolds numbers, it is well known that the flow in the wake area exhibits a large-scale wave motion [7, 9, 13]. Such a feature is also successfully reproduced in the current subcritical sphere case, as illustrated in Fig.13. Interestingly, as can be clearly observed in Fig.12, a progressive waviness is also pronounced in the wake area for the subcritical golf ball case. In addition, for both the golf ball and the smooth sphere, the typical wavelength of the wake flow structure spans approximately 6D in the current Reynolds number regime, which corresponds to the similar oscillation frequencies of the lateral force components in these two cases as shown in Fig.10 and Fig.11. Around the golf ball surface, the completely separated flow quickly becomes unstable in the shear layers and vortices are formed and shed distinctly. As the flow travels further downstream into the wake area, the hairpin-shape vortical structures appear to be apparent, as what is also observed in the wake flow of the smooth sphere.

Another interesting issue regarding the wave motion in the wake flow is whether the azimuthal position of the waviness-containing plane changes. For smooth spheres specifically, it was reported [7, 9, 13] that such a plane rotates randomly in time. In order to investigate the corresponding feature in the golf ball case, a time-dependent trace of the evolution of the instantaneous vortical structures behind the golf ball is provided in Fig.14. As revealed in the figure, the azimuthal position at which the wave motion is performed and the vortices are shed varies irregularly in time for the golf ball as well. Such characteristics again demonstrate that the influence of the surface roughness introduced by the dimples on the flow behaviors is somewhat limited in the subcritical regime.

3.3.2 Critical regime

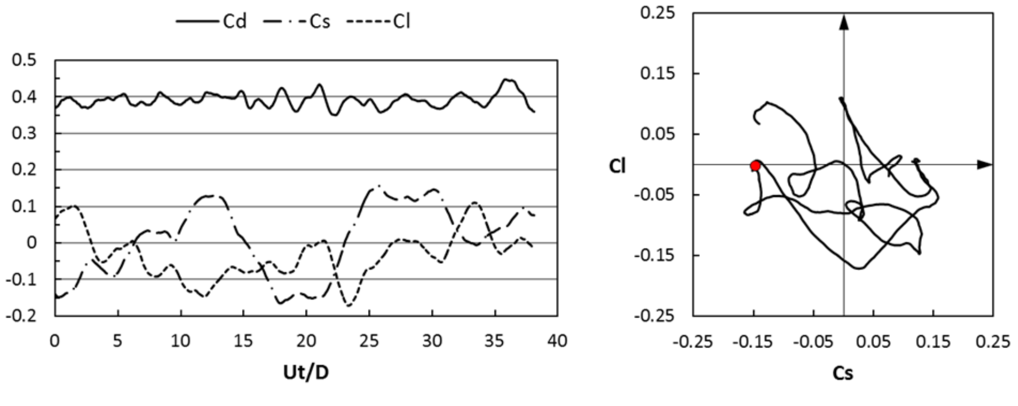

(a) (b)

Fig.15 Time series of the streamwise and lateral force coefficients for the golf ball at Re=7.5×10^4 after the flow reached statistically steady state: (a) temporal evolution of the drag coefficient Cd, side force coefficient Cs and lift coefficient Cl; (b) phase diagram of Cs and Cl, the red point represents the resultant lateral force at the non-dimensional moment indicated in Fig.17.

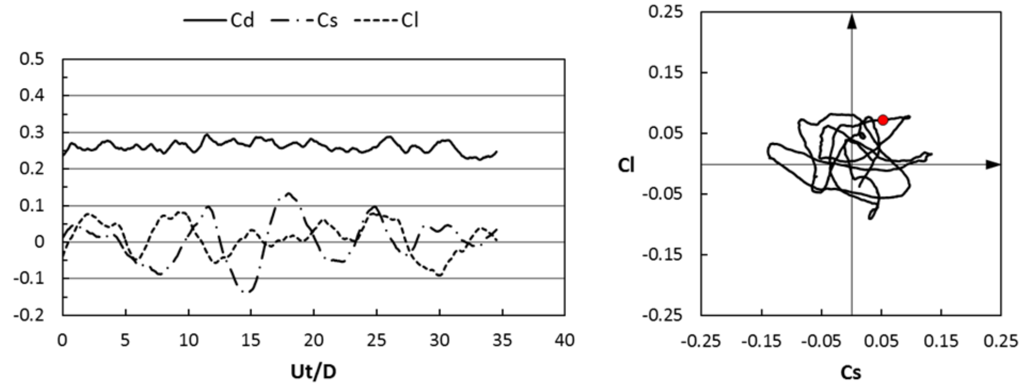

(a) (b)

Fig.16 Time series of the streamwise and lateral force coefficients for the smooth sphere at Re=2.0×10^5 after the flow reached statistically steady state: (a) temporal evolution of the drag coefficient Cd, side force coefficient Cs and lift coefficient Cl; (b) phase diagram of Cs and Cl, the red point represents the resultant lateral force at the non-dimensional moment indicated in Fig.18.

Fig.15 and Fig.16 display the time histories of the drag and the lateral force components in the critical Reynolds number range for the golf ball and the smooth sphere respectively. Compared with the subcritical case, the lateral force components acting on the golf ball appear to experience a larger oscillation at the critical Reynolds number. The standard deviations of both the side force and lift force coefficients exhibit values approximately twice as large as those of the subcritical results. Similar features are also apparent for the critical smooth sphere case. Moreover, one can observe that, for the smooth sphere, the non-dimensional frequencies of the lateral force variations in the critical regime are similar to those exhibited in the subcritical regime. For the golf ball, however, the corresponding oscillations display lower frequencies at the critical Reynolds number compared with the smooth sphere case. Concerning the direction of the resultant lateral force, it generally varies irregularly in time in both the golf ball case and the smooth sphere case. However, the changes of the side force and the lift force acting on the golf ball sometimes follow the opposite directions (i.e. the side force increases while the lift force decreases), which, interestingly, makes the curve of the total lateral force shown in Fig.15 (a) somewhat tilted along the direction parallel to the line Cl/Cs=-1.

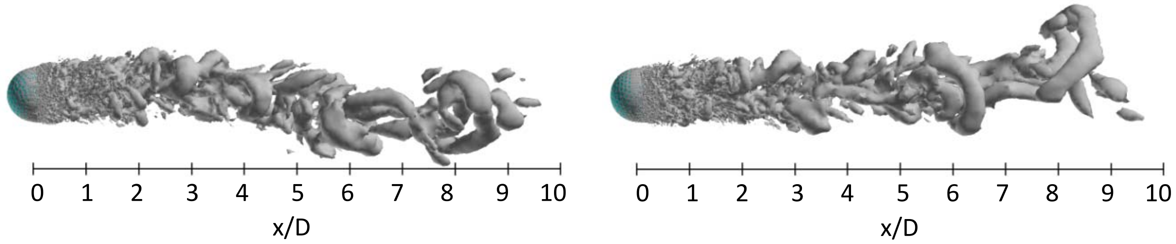

(a) x-y plane (b) x-z plane

Fig.17 Instantaneous vortical structures in the wake area of the golf ball at Re=7.5×10^4 (Ut/D=20.8, the resultant lateral force at this moment is indicated in Fig.15 (b) by the red point)

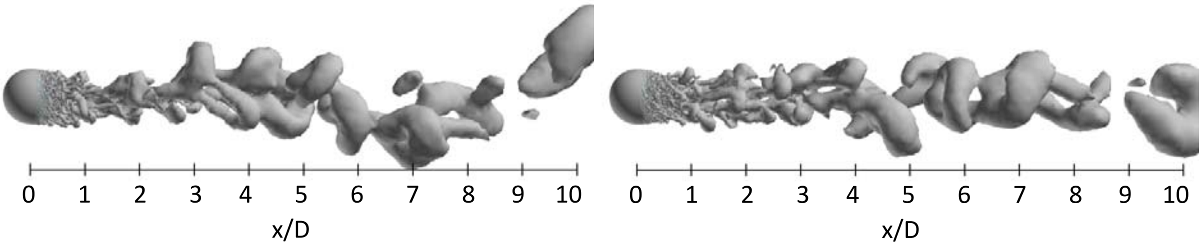

(a) x-y plane (b) x-z plane

Fig.18 Instantaneous vortical structures in the wake area of the smooth sphere at Re=2.0×10^5 (Ut/D=25.5, the resultant lateral force at this moment is indicated in Fig.16 (b) by the red point)

Provided in Fig.17 and Fig.18 are the instantaneous vortical structures respectively in the golf ball case and smooth sphere case at the corresponding critical Reynolds numbers. Somewhat apparent in both cases is the presence of the large-scale wave motions and the shed hairpin structures in the wake region. Agreeing with the experimental observation by Taneda [7], the typical wavelength of the wake oscillation in the critical smooth sphere case, spanning around 6D, stays similar to that exhibited in the subcritical regime, whereas a larger wavelength in the wake flow, spanning approximately 13D, is pronounced in the critical golf ball case corresponding to the relatively lower frequency of lateral force variation.

3.3.3 Supercritical regime

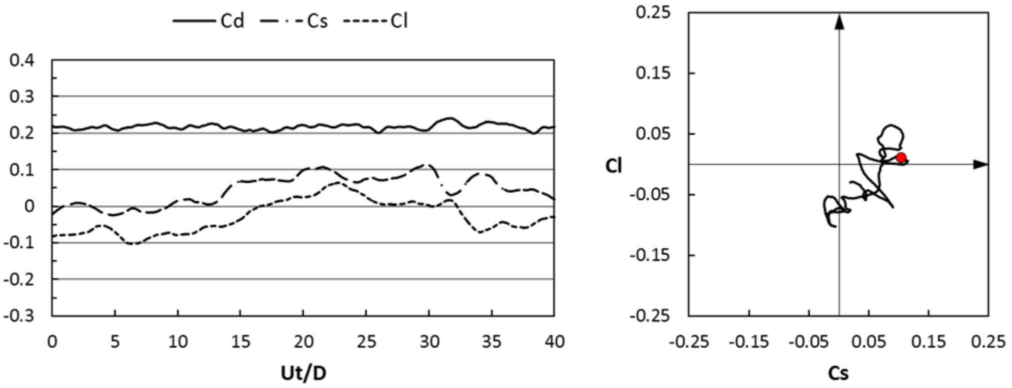

(a) (b)

Fig.19 Time series of the streamwise and lateral force coefficients for the golf ball at Re=1.1×10^5 after the flow reached statistically steady state: (a) temporal evolution of the drag coefficient Cd, side force coefficient Cs and lift coefficient Cl; (b) phase diagram of Cs and Cl, the red point represents the resultant lateral force at the non-dimensional moment indicated in Fig.21.

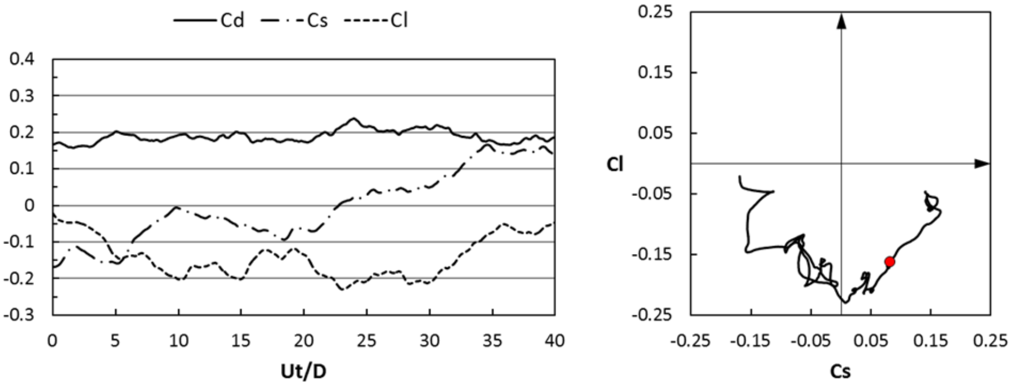

(a) (b)

Fig.20 Time series of the streamwise and lateral force coefficients for the smooth sphere at Re=1.14×10^6 after the flow reached statistically steady state: (a) temporal evolution of the drag coefficient Cd, side force coefficient Cs and lift coefficient Cl; (b) phase diagram of Cs and Cl, the red point represents the resultant lateral force at the non-dimensional moment indicated in Fig.22.

Displayed in Fig.19 and Fig.20 are the time histories of the drag and the lateral force components at the supercritical Reynolds numbers for the golf ball and the smooth sphere respectively. One can clearly observe that the oscillation of the lateral force acting on the golf ball exhibits a considerably smaller magnitude when compared to the oscillation of the lateral force acting on the smooth sphere. Meanwhile, compared with the respective critical results, the standard deviations of the lateral force components in the golf ball case decrease in the supercritical regime, whereas the variations of the corresponding statistics in the smooth sphere case follow an opposite trend. Concerning how the lateral force direction varies at the supercritical Reynolds numbers, unlike the corresponding behaviors observed in the subcritical and critical regimes, the curves which represent the evolution of the side force and the lift force barely intersect each other, at least within a long time interval, in both the golf ball and the smooth sphere cases. Such features interestingly result in a somewhat less random variation of the direction of the resultant lateral force for both models. As indicated in Fig.20 (b), the stationary smooth sphere placed in the supercritical flow is subjected to a nonzero lateral force during the whole time period, which agrees well with the conclusions by Taneda [7] and Constantinescu et al. [9]. Likewise, a similar phenomenon occurs to the stationary golf ball in the supercritical regime, as displayed in Fig.19 (b). However, it can be suggested from the pronounced differences between the lateral force development shown in Fig.19 (b) and Fig.20 (b) that the oscillation of the total lateral force is to some extent suppressed in the golf ball case when compared to the smooth sphere case. This phenomenon is assumed to be affected by the generation of the small-scale vortex on the golf ball surface. It is likely that the small-scale vortices prematurely induced by the dimples diffuse the momentum of the large-scale eddies and consequently weaken the large-scale vortex structures in the near-wall region behind the golf ball's rear surface, which is actually beneficial in the reduction of the lateral force oscillation.

Shown in Fig.21 and Fig.22 are the instantaneous vortical structures in the supercritical wake flow of the golf ball and the smooth sphere respectively. As is apparent in the figures, the large-scale vortex shedding appears in both the wake flow of the smooth sphere, which agrees well with the report by Constantinescu et al. [9], and the wake flow of the golf ball. In the near-wall region behind the smooth sphere, the flow appears to be severely twisted due to a strong oscillation, and a considerable lateral force is in turn generated on the sphere. As the flow travels further downstream, the completely asymmetric wake structures are formed, which significantly deviate from the streamwise axis that goes across the center of the sphere (x axis). The orientation of the asymmetry of the wake flow corresponds to the instantaneous direction of the resultant lateral force acting on the sphere. By comparison, the flow in the near-wall region behind the golf ball exhibits a visibly weaker oscillation. A less twisted pattern of the near-wall flow is formed, as illustrated in Fig.21, and the obviously smaller lateral force is imposed on the golf ball. The shed vortical structures travel into the further downstream area approximately following the direction which is parallel to the streamwise axis that goes across the center of the golf ball (x axis), despite a slight tilt corresponding to the small instantaneous lateral force acting on the golf ball, as can be observed in Fig.21 (a).

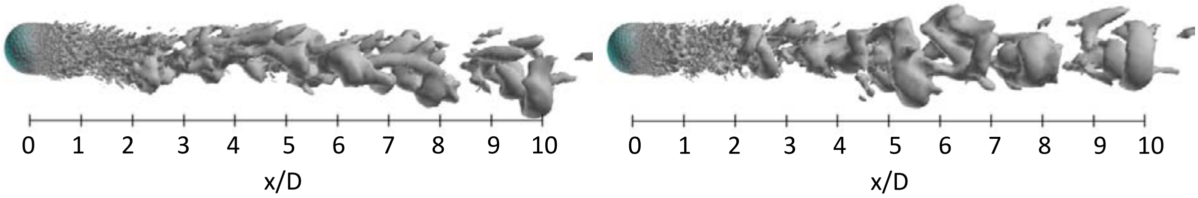

(a) x-y plane (b) x-z plane

Fig.21 Instantaneous vortical structures in the wake area of the golf ball at Re=1.1×10^5 (Ut/D=28.9, the resultant lateral force at this moment is indicated in Fig.19 (b) by the red point)

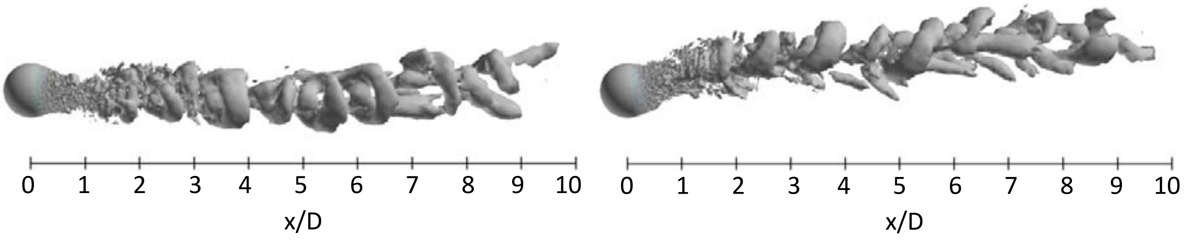

(a) x-y plane (b) x-z plane

Fig.22 Instantaneous vortical structures in the wake area of the smooth sphere at Re=1.14×10^6 (Ut/D=31.9 the resultant lateral force at this moment is indicated in Fig.20 (b) by the red point)

Further insight into the differences between the wake structures in the two supercritical cases are provided in Fig.23 and Fig.24 by the investigation of the streamwise vorticity component ω_x (normalized by multiplying D/U, where D is the diameter and U is the incoming flow velocity) in planes normal to the freestream direction, displayed at 1.5D and 3.0D from the center of the golf ball and the smooth sphere. At x/D=1.5, a pair of counter-rotating vortices is evident in the smooth sphere case. Between the twin vortices a momentum normal to a line connecting the center of each vortex is generated, which corresponds to the lateral force acting on the sphere in the opposite direction. On the other hand, vortices with more random patterns are distributed behind the golf ball at the same dimensionless downstream location. Moreover, one can clearly observe at this location that the pair of vortices considerably deviates from the x axis, whereas the structures behind the golf ball stay more concentrated and approximately symmetrical around the center of the golf ball. At the location further downstream (x/D=3.0), the pair of vortices becomes even further away from the center of the smooth sphere, whereas the corresponding vortices in the golf ball case remain concentrated and distributed close to the center of the golf ball in spite of a relatively larger asymmetry of the structures affected by the lateral force. The twin streamwise vortices and their deviation from the x axis as going downstream clearly explain the continuous lateral forces and their differences between the smooth sphere and the golf ball as indicated in Fig.19 and Fig.20.

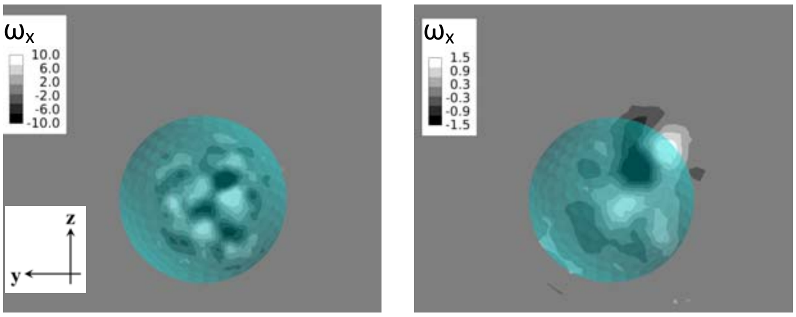

(a) x/D=1.5 (b) x/D=3.0

Fig.23 Streamwise vorticity component in the wake flow of the golf ball viewed in the crossflow plane at x/D=1.5 and x/D=3.0; Re=1.1×10^5 (Ut/D=28.9)

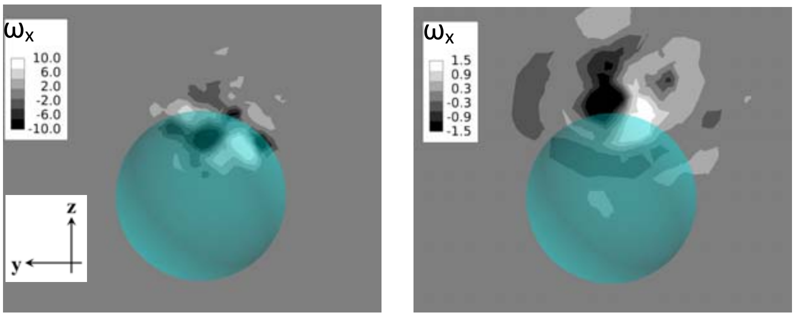

(a) x/D=1.5 (b) x/D=3.0

Fig.24 Streamwise vorticity component in the wake flow of the smooth sphere viewed in the crossflow plane at x/D=1.5 and x/D=3.0; Re=1.14×10^6 (Ut/D= 31.9)

4 Conclusions

Large-eddy simulations have been conducted to study the flow over a golf ball in the subcritical (Re=4.3×10^4), critical (Re=7.5×10^4) and supercritical (Re=1.1×10^5) regimes. A direct comparison of characteristics of flow fields was made between the current golf ball and the smooth sphere model used by Muto et al. [10] in the corresponding Reynolds number regimes. Particular attention was paid to the effect of the golf ball dimples on the evolution of lateral forces and the formation of wake structures.

The statistical features obtained in this work, such as the drag coefficient and surface pressure distribution, show a very good agreement with the previous experimental and numerical results. The drag crisis of the golf ball is successfully captured at a relatively lower Reynolds number range compared to the smooth spheres. The phenomenon of the local flow separation and reattachment inside the dimples and the consequent momentum transfer in the near-wall region is also accurately reproduced in the present study. This mechanism is considered as the key factor contributing to the drag crisis of a golf ball [2-3].

In the subcritical regime, the magnitude and the direction of the resultant lateral force change irregularly in time for both the golf ball and the smooth sphere. Also, the large-scale wave motion is pronounced in the wake areas of both models, and the wavelengths are comparable. The azimuthal position of the waviness-containing plane varies irregularly in time for the golf ball, which is consistent with the corresponding conclusions of smooth spheres [7, 9, 13].

In the critical regime, for both the golf ball and the smooth sphere, the lateral force oscillation exhibits a larger magnitude compared with the subcritical cases, and the direction of the resultant lateral force differs irregularly in time. In the golf ball case, a larger wavelength is displayed in the wake flow's wave motion owing to the relatively lower frequency of lateral force variation compared with the smooth sphere case.

In the supercritical regime, both the golf ball and the smooth sphere appear to be subjected to a nonzero lateral force during a long time interval, although the magnitude of the lateral force acting on the golf ball is considerably smaller when compared to the smooth sphere. The wake structures behind the smooth sphere show a significant deviation from the streamwise axis that goes across the center of the sphere, whereas the wake structures behind the golf ball stay closer to the corresponding axis through the center of the golf ball. Examination of the streamwise vorticity component in the wake area reveals the presence of the pair of counter-rotating vortices behind the smooth sphere. Such twin streamwise vortices and their remarkable offset from the x axis significantly contribute to the considerable lateral force acting on the smooth sphere. On the other hand, the vortices behind the golf ball exhibit a more concentrated distribution around the x axis, though with more random patterns. The less asymmetry of the wake structures corresponds to the somewhat suppressed lateral force acting on the golf ball.

Extensions of the current contribution will be made for the next step. Specifically, the self-spinning motion will be imposed on both the golf ball and smooth sphere. Particular attention will be focused towards how the dimples affect the generation of lift force under self-rotating conditions. The mechanism of the inverse Magnus effect on the golf ball [1, 25] and its comparison with the smooth sphere will be investigated in detail.

Acknowledgments This work was supported by following grants: "Strategic Programs for Innovative Research" Field No. 4: Industrial Innovations from the Ministry of Education, Culture, Sports, Science, and Technology (MEXT)'s "Development and Use of Advanced, High-Performance, General-Purpose Supercomputers Project" and carried out in partnership with the University of Tokyo for the improvement of FrontFlow/red-Aero for High Performance Computing simulation; "Revolutionary Simulation Software (RSS21)" by MEXT for the development of FrontFlow/red; Japan Society for the Promotion of Science (JSPS) Grant-in Aid for Scientific Research (KAKENHI) (B) Number 26289033 for the physical mechanism of surface roughness and its separation. Computational resources were provided by following supercomputer systems: HITACHI SR16000 M1 at Hokkaido University; HITACHI HA8000-tc/HT210 at Kyushu University and Dell PowerEdge R620 at Center for Research on Innovative Simulation Software, Institute of Industrial Science, University of Tokyo.

References

1. Bearman, P.W., Harvey, J.K.: Golf ball aerodynamics. Aeronaut. Q. 27, 112-122 (1976)
2. Choi, J., Jeon, W., Choi, H.: Mechanism of drag reduction by dimples on a sphere. Phys. Fluids. 18, 041702.1-041702.4 (2006)
3. Smith, C.E., Beratlis, N., Balaras, E., Squires, K., Tsunoda, M.: Numerical investigation of the flow over a golf ball in the subcritical and supercritical regimes. International Journal of Heat and Fluid Flow. 31, 262-273 (2010)

4. Achenbach, E.: Experiments on the flow past spheres at very high Reynolds numbers. J. Fluid Mech. 54, 565-575 (1972)
5. Mehta, R.D., Pallis, J.M.: Sports ball aerodynamics: effects of velocity, spin and surface roughness. Minerals, Metals and Materials Society/AIME, Materials and Science in Sports (USA), 185-197 (2001)
6. Achenbach, E.: Vortex shedding from spheres. J. Fluid Mech. 62, 209-221 (1974)
7. Taneda, S.: Visual observations of the flow past a sphere at Reynolds numbers between 10^4 and 10^6. J. Fluid Mech. 85, 187-192 (1978)
8. Sakamoto, H., Haniu, H.: A study on vortex shedding from spheres in a uniform flow. Journal of Fluids Engineering. 112, 386-392 (1990)
9. Constantinescu, G., Squires, K.: Numerical investigations of flow over a sphere in the subcritical and supercritical regimes. Phys. Fluids. 16(5), 1449-1465 (2004)
10. Muto, M., Tsubokura, M., Oshima, N.: Negative Magnus lift on a rotating sphere at around the critical Reynolds number. Phys. Fluids. 24, 014102.1-014102.15 (2012)
11. Davies, J.M.: The aerodynamics of golf balls. Journal of Applied Physics. 20, 821-828 (1949)
12. Moin, P., Kim, J.: Tackling turbulence with supercomputers. Scientific American. 276(1), 46-52 (1997)
13. Yun, G., Kim, D., Choi, H.: Vortical structures behind a sphere at subcritical Reynolds numbers. Phys. Fluids. 18, 015102.1-015102.14 (2006)
14. Norman, A.K., McKeon, B.J.: Unsteady force measurements in sphere flow from subcritical to supercritical Reynolds numbers. Experiments in Fluids. 51(5), 1439-1453 (2011)
15. Norman, A.K., McKeon, B.J.: The effect of a small isolated roughness element on the forces on a sphere in uniform flow. Experiments in Fluids. 51(4), 1031-1045 (2011)
16. Norman, A.K., Kerrigan, E.C., McKeon, B.J.: The effect of small-amplitude time-dependent changes to the surface morphology of a sphere. J. Fluid Mech. 675, 268-296 (2011)
17. Perry, A.E., Lim, T.T.: Coherent structures in coflowing jets and wakes. J. Fluid Mech. 88(03), 451-463 (1978)
18. Perry, A.E., Lim, T.T., Chong, M.S.: The instantaneous velocity fields of coherent structures in coflowing jets and wakes. J. Fluid Mech. 101(02), 243-256 (1980)
19. Perry, A.E., Tan, D.K.M.: Simple three-dimensional vortex motions in coflowing jets and wakes. J. Fluid Mech. 141, 197-231 (1984)
20. Germano, M., Piomelli, U., Moin, P., Cabot, W.H.: A dynamic subgrid-scale eddy viscosity model. Phys. Fluids A. 3(7), 1760-1765 (1991)
21. Tsubokura, M., Nakashima, T., Kitoh, K., Sasaki, Y., Oshima, N., Kobayashi, T.: Development of an unsteady aerodynamic simulator using large-eddy simulation based on high-performance computing technique. SAE Technical Paper. No.2009-01-0007 (2009)
22. Schlichting, H.: Boundary Layer Theory. McGraw-Hill, New York (1955)
23. Wieselsberger, C.: Weitere Feststellungen uber die Gesetze des Flussigkeits und Luftwiderstandes. Phys. Z. 23, 219-224 (1922)
24. Hunt, J.C.R., Wray, A.A. and Moin, P.: Eddies, streams, and convergence zones in turbulent flows. Center for Turbulence Research Report. CTRS88, 193-208 (1988)
25. Beratlis, N., Squires, K., Balaras, E.: Numerical investigation of Magnus effect on dimpled spheres. Journal of Turbulence. 13(15), 1-15 (2012)